Electronic Supplementary Information for

Highly Active Hydrogen Evolution Catalysis from Metallic WS_2 Nanosheets

*Mark A. Lukowski, Andrew S. Daniel, Caroline R. English, Fei Meng, Audrey Forticaux, Robert J. Hamers, and Song Jin**

I. Experimental Details and methods

All chemicals were purchased from Sigma-Aldrich and used as-received unless otherwise noted.

Synthesis of WS_2 nanostructures. Tungsten foils (0.05 mm thick, ~ 1 cm^2) were cleaned by sonication in acetone, isopropyl alcohol, and 18 MΩ deionized water for 10 min each before they were dried using nitrogen flow. Recycled tungsten substrates were first etched in aqua regia (3:1 concentrated HCl: concentrated HNO_3) for 10 min to remove remnant materials and ensure a consistent reaction substrate. In a home-built chemical vapor deposition (CVD) reactor consisting of a 1-inch diameter fused silica tube equipped with pressure and gas flow controls placed in a single-zone tube furnace, an alumina combustion boat containing 50 mg tungsten chloride (WCl_6, 99.9 %) and 200 mg elemental sulfur (99.5 %) was placed outside of the tube furnace upstream of the prepared tungsten substrates. The reactor was evacuated and flushed three times with argon before it was back filled to the set-point pressure of 770 Torr under an argon flow of 125 sccm and heated to 550 ^oC. The combustion boat was pushed 1.5 cm into the furnace using a magnet and hydrogen flow was started at 0.75 sccm to initiate the reaction which lasted 20 min, then the furnace was cooled naturally under an argon flow.

***n*-Butyllithium exfoliation treatment and isolation.** Inside an argon-filled glove box, the tungsten foil or graphite substrates covered with as-synthesized WS_2 nanostructures were soaked in 3 mL *n*-butyllithium solution (2.7 M in heptane) inside sealed vials, which were then brought out of the glove box and heated to 80 ^oC inside an oven for 48 h. Alternatively, microwave-assisted intercalation reactions were carried out using a CEM Discover and Explorer microwave heater equipped with an infrared temperature probe and control used to maintain the reaction temperature at 80 ^oC for 20 min using approximately 200 W power. After heating, the *n*-butyllithium solutions were often slightly yellow and cloudy in appearance, signifying the presence of oxidized species. For both intercalation reaction

methods, excess *n*-butyllithium was removed by rinsing the intercalated samples 2-3 times with dry heptane. Then the samples were reacted with excess 18 MΩ deionized water which caused violent evolution of H_2 gas. The solution immediately turned black, as the WS_2 nanosheets delaminated from the substrate and dispersed into the solution. The resulting slurry was centrifuged in an Eppendorf 5415D tabletop centrifuge at 13,200 rpm for 15 min. The supernatant was removed and this washing procedure was repeated twice more with 18 MΩ deionized water to ensure complete reaction of intercalated lithium before the nanosheets were suspendended in ~1 mL of isopropyl alcohol.

For comparison, bulk WS_2 powder (99 %, 2 μm particle size) was also used as the starting material for the exfoliation reactions. 300 mg of the bulk powder was added to 4 mL of *n*-butyllithium solution in heptane (2.7 M) and subjected to both methods of heating: microwave-assisted heating for 20 min at 80 ^oC (see the descriptions above), or 48 h in an oven at 100 ^oC in a teflon lined autoclave. The products were then washed and reacted with water following the procedures described above with similar appearance changes observed. For the more thoroughly intercalated samples that had been heated to 100 ^oC for 48 h, to make sure all of the large micron-sized WS_2 particles are intercalated thouroughly and completely exfoliated, it was assumed that any smaller exfoliated WS_2 flakes would migrate to the top of the solution, while the larger particles would settle to the bottom of the reaction vessel. Therefore, the top half of the supernant solution was separated and centrifuged down as described above. These smaller particles were then suspended in isopropanol and drop-casted onto a graphite substrate and electrochemically tested, and called "supernatent“ WS_2 nanosheets in Figure S7. Those exfoliated materials collected from the bottom were also drop-casted, examined and tested, and they are called “everything“ WS_2 nanosheets in Figure S7. The fact the electrochemical behaviors, the SEM, and the Raman spectra did not reveal much difference between the supernant and everything WS_2 nanosheet samples suggests that these samples are indeed thorougly exfoliated. However, they still did not perform as well as the exfoliated nanostructures originated from WS_2 nanostructures grown by CVD (Figure S7).

Structural characterization. SEM was performed using a LEO Supra55 VP microscope operating at 3 kV. PXRD data were collected on harvested nanostructures dispersed on glass substrates using a Bruker D8 advanced powder diffractometer with Cu Ka radiation and the background from glass substrate was subtracted. TEM samples were prepared by gentle sonication and drop-casting onto lacey carbon supported TEM grids. HRTEM of the WS_2 nanostructures and nanosheets was performed using an aberration-corrected FEI Titan

scanning transmission electron microscope operated at an accelerating voltage of 200 kV in TEM mode. Raman spectra were taken using a Thermo Scientific DXR confocal Raman microscope using a 532 nm excitation laser. AFM measurements were taken on samples cast onto evaporated gold (50 nm) on Si(100)/SiO_2 substrates using an Agilent 5500 AFM equipped with current-sensing capabilities using a symmetric Pt coated tip (30 nm, miikroMasch) with a force constant of 2.7 N/m. All of the data were collected in the trace, with no significant hysteresis in the retrace, as current-sensing requires the AFM to be operated in contact mode. X-ray photoelectron spectroscopy (XPS) was performed on a custom-built XPS system (Phi Electronics, Eden Prairie, MN), that included a model 10-610 Al K_α x-ray source (1486.6 eV photon energy) and a model 10-420 toroidal monochromator. A model 10-360 hemispherical analyzer with a 16-channel detector array was used that under effective operating conditions had an analyzer resolution of 0.4 eV. Electrons were collected at an emission angle of 45° from the surface normal of the sample. High resolution data was collected for W4*f*, S2*p*, O1*s*, C1*s* and Au4$f_{7/2}$. The high resolution data were shifted so that the Au4$f_{7/2}$ peak for all samples was at 84.0 eV and fit to Voigt functions in order to determine binding energies. Since the Au4$f_{7/2}$ was from the underlying substrate, we verified no charging effects were present in our data by also comparing the adventituous C1*s* peaks. Ultraviolet photoelectron spectroscopy (UPS) was performed on the same custom-built system used to perform XPS. The analyzer resolution for UPS measurements was 0.09 eV. Negative biases were applied to the samples to overcome the work function of the analyzer. A linear background correction was applied to the UPS data before any data workup. Platinium foil was used to determine the Fermi level for the system by fitting the valence band edge of the platinum UP spectra to the Fermi function. The UPS spectra were then shifted to account for the negative bias applied as well as to place E_F equal to 0 eV. The valence band edge for the WS_2 samples were fit to lines and the x-axis intercept was used to determine the valence band maximum for each sample.

Electrochemical characterization. Electrochemical measurements were performed using a rotating disk electrode (BASi, RDE-2) in a three-electrode electrochemical cell using a Bio-Logic SP-200 potentiostat. All measurements were performed in 50 mL of 0.5 M $H_2SO_{4(aq)}$ electrolyte (pH = 0.16) prepared using 18 MΩ deionized water and constantly purged with H_2 gas (99.999%), using various WS_2 nanostrures deposited on graphite disks as the working electrode, a graphite rod as a counter electrode, and a saturated calomel (SCE) reference electrode (CH Instruments). For preparing the working electrodes, spectroscopically pure

graphite rods (99.9995%, Ultra F purity, Ultra Carbon Corporation) cut into thin disks (6 mm diameter; ~0.4 mm thick) were polished to a near-mirror finish using abrasive cloths. They are sonicated subsequently in 18 MΩ deionized water for 10 min, then in aqua regia (3:1 concentrated HCl: concentrated HNO_3) for 10 min (to remove remnant metal impurities), and then in 18 MΩ deionized water for 10 min again, before they were dried in an oven at 120 ^oC for 20 min. Such graphite disks have a geometric area of 0.283 cm^2. The WS_2 cast onto graphite disks (2 × 3 μL drops) were mounted on top of the embedded glassy carbon RDE electrodes using colloidal silver paint (Ted Pella). The amount of the catalyst loading was estimated using quartz crystal microbalance (QCM) (Q-Sense E4 instrument, Biolin Scientific, Stockholm, Sweden) measurements, in which 2 × 3 μL drops of the same WS_2 nanosheet suspension in isopropyl alcohol were dropcasted onto the surface of the SiO_2-coated quartz crystal sensor (QSX 303, Q-Sense, 50 nm SiO_2, surface area 1.04 cm^2) and the QCM freqency change was read off after the frequency stabilized (i.e. the solvent was fully evaporated). Based on 3 measurements, the average total solid mass deposited was calculated to be 0.29±0.05 mg using the Sauerbrey relationship. This yielded an estimated catalyst loading of 1.0±0.2 mg/cm^2 onto the graphite disk with a geometric area of 0.283 cm^2.

As a comparison, a standard Pt disc (4 mm diameter, Ted Pella) was mounted to the glassy carbon RDE electrode using the same method. The reversible hydrogen electrode (RHE) was calibrated using platinum as both working and counter electrodes to +0.260 V vs. the SCE reference. The performance of the hydrogen evolution catalysts was measured using linear sweep voltammetry beginning at +0.30 V and ending at −0.45 V vs. RHE with a scan rate of 3 mV/s when the working electrode is rotated at 2000 rpm. As-grown 2H-WS_2 nanostructures grown directly on graphite disks and harvested 2H-WS_2 nanostructures drop-cast onto graphite disks exibited similar catalytic activities.

Electrochemical impedance spectroscopy was performed when the working electrode was biased at a constant –0.250 V vs. RHE while sweeping the frequency from 5 MHz to 10 mHz with a 10 mV AC dither. The impedance data were fit to a simplified Randles circuit to extract the series and charge transfer resistances. Cyclic voltammograms taken with various scan rates (20, 40, 60, 80, 100, 120, 140, 160, 180 mV/s) were collected in the 0.1–0.2 V vs. RHE region and were used to estimate the double-layer capacitance. The electrochemical stability of the catalysts was evaluated by cycling the electrode 500 times; each cycle started at +0.10 V and ended at −0.45 V vs. RHE with a scan rate of 50 mV/s while rotating the working electrode at 2000 rpm.

II. Raman spectroscopy and powder X-ray diffraction characterization

Raman spectroscopy (Figure S1a) reveals the characteristic peaks (352 cm^{-1} and 421 cm^{-1}) for as-grown WS_2 nanostructures corresponding to the E^1_{2g} and A_{1g} modes of 2H-WS_2, respectively.[20] After chemical exfoliation, these peaks are severely diminished and broadened, which is consistent with past reports on 1T-WS_2[6c, 14] and our own past studies on 1T-MoS_2.[6a] Interestingly, we observe a peak (256 cm^{-1}) in the Raman spectrum that corresponds to tungsten oxide in the exfoliated nanosheets prepared by microwave-assisted intercalation. This reflects the air contamination that likely results from the imperfect seal of the microwave reaction vessel. PXRD reveals phase-pure 2H-WS_2 in the as-grown nanostructures, with muted reflections after chemical exfoliation (Figure S1b). The muted (00*l*) reflections reflect the efficient exfoliation of the material into the 1T-WS_2 polymorph, but the presence of the (002) reflection especially reflects the propensity of the nanosheets to restack into their thermodynamically favoured 2H phase.[12b, 12c]

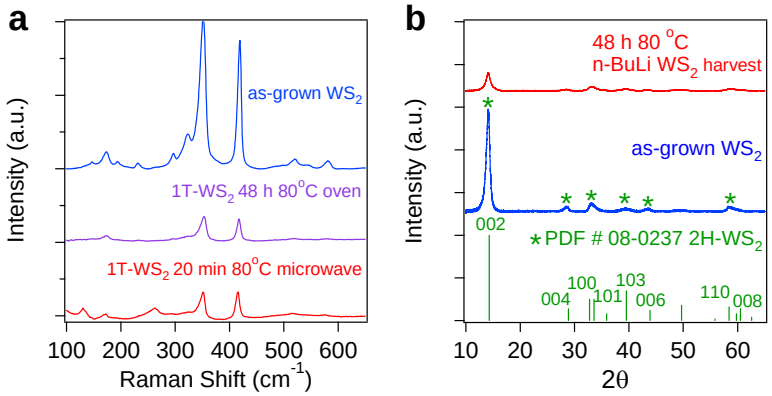

Figure S1. (a) Raman spectra and (b) PXRD patterns for the as-grown WS_2 nanostructures and chemically exfoliated WS_2 nanosheets.

III. Additional details for X-ray photoelectron spectroscopy (XPS)

We used XPS to reveal the chemical differences between the as-grown and chemically exfoliated WS_2 nanosheets. These samples were prepared by drop-casting harvested 1T- and 2H-WS_2 nanostructures directly onto gold-coated silicon substrates. Special care was taken to limit their exposure to atmosphere due to concerns of surface oxidation or contamination. All XPS data were aligned by defining the observed Au4$f_{7/2}$ peak from the substrate as 84.0 eV (Figure S2a). We also used the C1*s* peak (Figure S2b) to make sure the data are still aligned and the samples are not experiencing differential charging effects that may convolute the data. Electron transfer from intercalated lithium favours the octahedral coordination of the

metal atoms, and therefore causes the structural transition from the 2H to 1T polymorph. The electronic structure modifications that accompany the phase change should be detectable by XPS. As shown in the main text, the presence of new chemical species with lower binding energies can be readily attributed to the 1T polymorph.

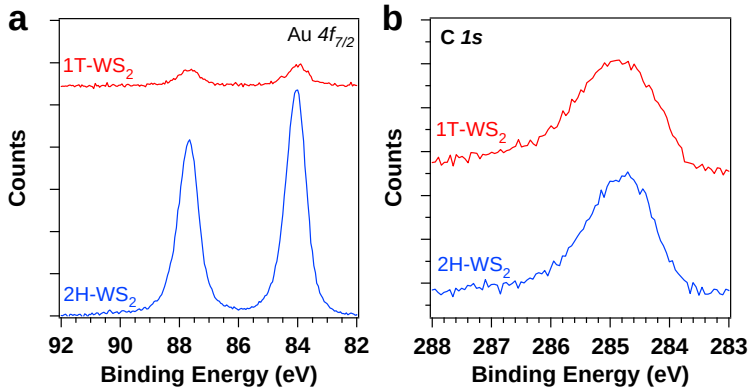

Figure S2. X-ray photoelectron spectra of the (a) Au4*f* and (b) C1*s* regions used for the alignment of all XPS data shown in Figure 2 in the main text. All binding energies reported were manually shifted so that the Au4$f_{7/2}$ peak fell at 84.0 eV. The adventitious carbon in the C1*s* region was then used to verify that any charging effects present at the sample surface were accounted for in our shifts.

IV. Current-sensing atomic force microscopy (CSAFM)

We characterized the as-grown and chemically exfoliated WS_2 nanosheets drop-casted on evaporated gold (50 nm) film on silicon (100) substrates using an Agilent 5500 series AFM with current-sensing capabilities using a symmetric Pt coated tip (30 nm, MikroMasch) with a force constant of 2.7 N/m. The topography (Figure S3a, e), deflection (Figure S3b, f), and friction (Figure S3c, g) images were collected simultaneously with their corresponding conductivity maps (Figure S3d, h). All of the data were taken in contact mode with the sample held at a constant bias of +20 mV and all images are 2 µm by 2 µm. The presence of WS_2 on the substrates for the 2H- and 1T samples is confirmed by the topography, deflection, and friction images which show clear textures. The current-sensing maps illustrate the striking difference in material conductivity: the 1T-WS_2 sample is uniformly conducting, but the inhomogeneous (speckled) appearance of the 2H sample reflects the more insulating nature of 2H-WS_2. This further confirms that the lithium intercalation and exfoliation treatment results in a semiconducting to metallic phase transition, and there is also

effective electrical connection between the exfoliated metallic 1T-WS_2 nanosheets and the conducting substrate.

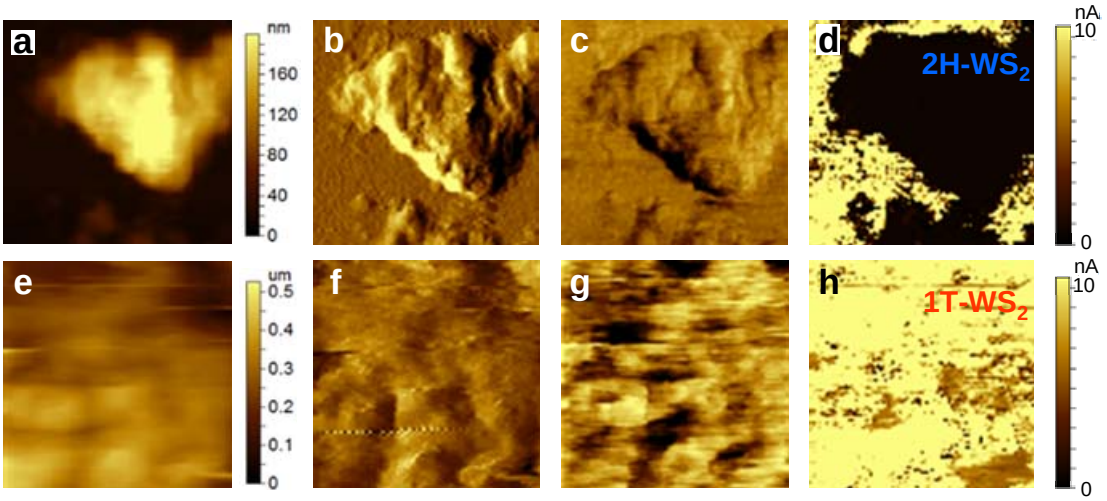

Figure S3. Topography, deflection, friction, and conductivity AFM maps of (a-d) semiconducting 2H-WS_2 nanostructures and (e-h) exfoliated metallic 1T-WS_2 nanosheets both drop-casted onto evaporated gold film on silicon (100) substrates. All images are 2 µm x 2 µm. Deflection and friction images have arbitrary relative scales.

V. Dependence of catalytic activity on microwave intercalation conditions

The catalytic performance of the exfoliated 1T-WS_2 nanosheets was examined as a function of the duration of microwave-assisted intercalation (Figure S4). The as-synthesized WS_2 nanostructures on tungsten foils from the same CVD synthesis were mircrowaved in 2.7 M *n*-butyl lithium in heptane at 80 ^{o}C for 10, 20, 30, and 60 min before rinsing away the excess *n*-butyl lithium with dry hexane/heptane, and subsequently reacting them with excess 18 MΩ deionized water, thus removing the intercalated lithium and exfoliating the WS_2 nanosheets. This causes the full delamination of the exfoliated WS_2 nanosheets from the W foils so that they can be harvested and isolated by centrifugation. Significant improvement in catalytic performance compared to the as-grown WS_2 nanostructures are observed for samples from all intercalation conditions. However, prolonged microwave-assisted intercalation reactions (60 min) produced less catalytically active materials, possible due to the oxidation of the 1T-WS_2 nanosheets. Therefore, we chose 20 min as the standard microwave-assisted intercalation time at 80^{o}C for the balence of performance and reaction efficiency.

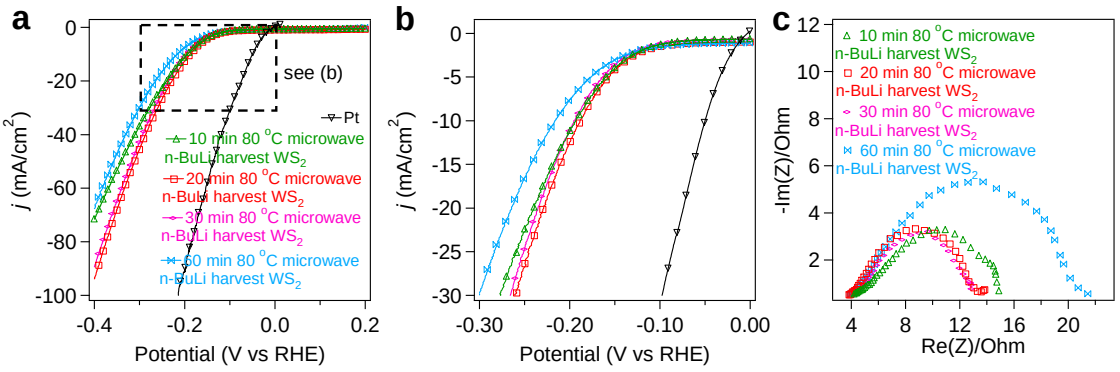

Figure S4. Polarization curves showing the (a) overall catalytic activity and (b) performance at lower potentials as a function of microwave intercalation duration at 80 °C in 2.7 M *n*-butyl lithium in heptane. (c) Nyquist plots show the corresponding trends in electrode kinetics for the same set of samples.

VI. Chemical exfoliation of WS_2 nanostructures synthesized directly on graphite

Following the success of our recent 1T-MoS_2 work, we initially tried the analogous exfoliation approach in which as-grown WS_2 nanostructures synthesized directly on graphite disks were chemically exfoliated and then directly tested for catalysis. However, for intercalated WS_2 nanostructures, the violent H_2 generation caused the nanosheets to delaminate from the substrates entirely. This was observed visually, and further confirmed by their very poor electrocatalytic performance (Figure S5), in contrast to the optimized harvest and drop-cast approach discussed in the main text. In fact, the delamination of the WS_2 materials is so severe that the HER catalytic performance is even worse than the as-grown 2H-WS_2 on graphite substrates.

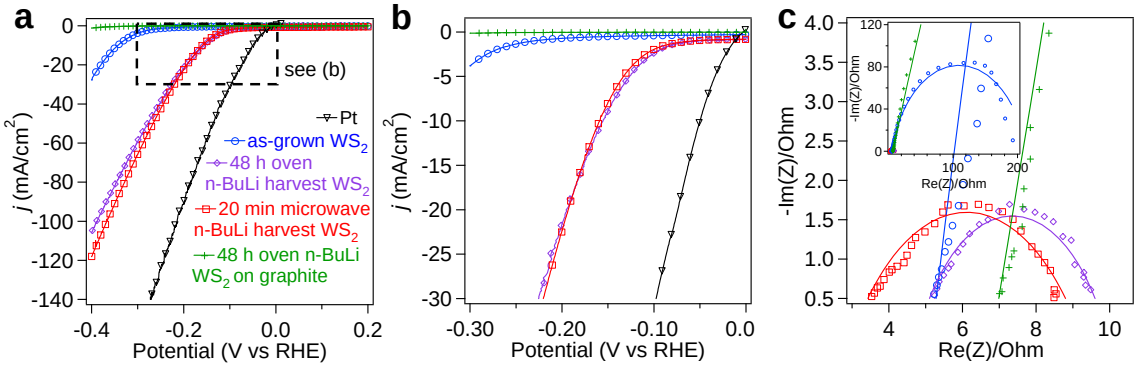

Figure S5. Polarization curves comparing the (a) overall catalytic activity and (b) performance at lower potentials for chemically exfoliated WS_2 nanosheets obtained by

various approaches. (c) Nyquist plots show the corresponding trends in electrode kinetics for the same set of samples.

VII. Comparison of exfoliated WS_2 nanosheets made from bulk WS_2 powder and CVD grown WS_2 nanostructures

This importance of starting with the well-controlled WS_2 nanostructures synthesized by our CVD method for chemical exfoliation is demonstrated by the superior HER catalytic performance of the resulting exfoliated metallic WS_2 nanosheets as compared to the nanosheets exfoliated from commercially available bulk WS_2 powder that have been subjected to the same intercalation conditions (20 min microwave-assisted reaction at 80 ^{o}C) and exfoliation treatment (Figure S6a, b). This is also supported by comparing the catalytic activity of the CVD grown nanostructures with the as-received bulk powder without the exfoliation treatment. Electrochemical impedance spectroscopy (EIS) shows that intercalation and exfoliation of the bulk powder result in behaviors most similar to the as-grown CVD synthesized WS_2 nanostructures *before exfoliation* (Figure S6c). Data fittings to a simplified Randles circuit reveal charge transfer resistances (R_{ct}) of 1919 Ω for the as-received bulk WS_2 powder and 192 Ω for the "exfoliated“ bulk powder, in comparison with the 200 Ω for the CVD synthesized WS_2 before exofliation. In contrast, the exfoliated 1T-WS_2 nanosheets from the CVD synthesized nanostructures exhibit much more facile kinetics (R_{ct} = 5 Ω), as shown in Figure 3c and discussed in the main text. The dramatic difference in catalytic activity can likely be explained by the incomplete lithiation, conversion, and exfoliation of the larger and irregular particles (~ 2 μm) in the bulk WS_2 powder. SEM images of the as-received (Figure S6d) and the "exfoliated" bulk powder (Figure 6e) further support this hypothesis. Raman spectroscopy and PXRD also show only small differences in the "exfoliated" material as compared to the as-received bulk powder, thereby suggesting that much of the powder has not been transformed to the more catalytically active 1T polymorph. These results underlines the benefits of using the CVD synthesized WS_2 nanomaterials with few layers and small crystallite size, as they require much shorter intercalation times in order to achieve efficient conversion and subsequent exfoliation of 1T-WS_2 nanosheets.

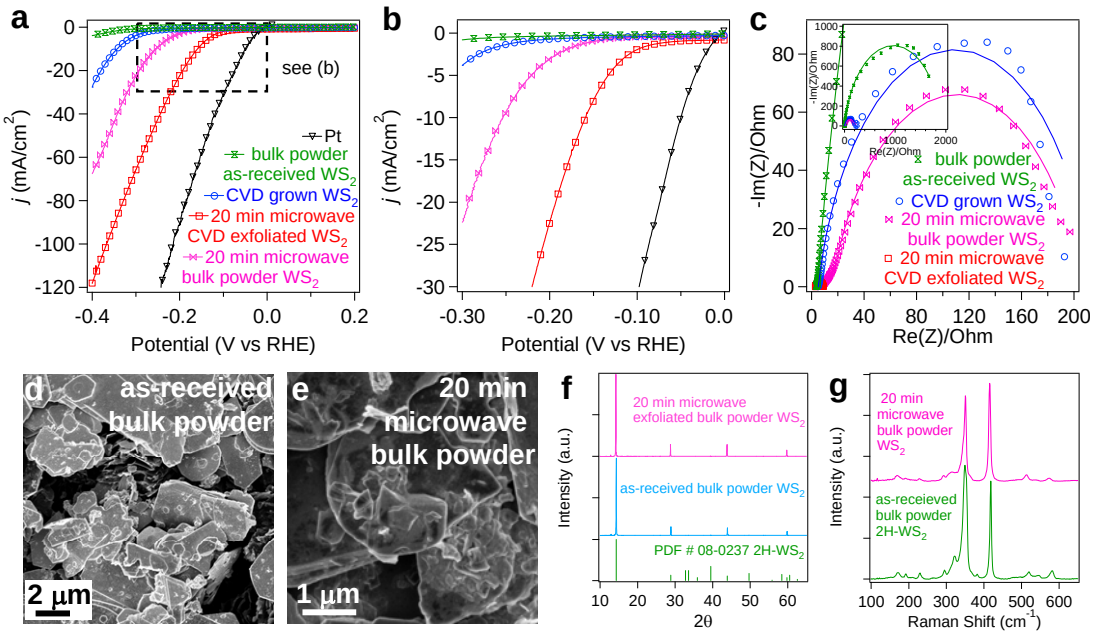

Figure S6. Polarization curves showing the superior (a) overall catalytic activity and (b) performance at lower potentials for chemically exfoliated nanosheets produced from CVD synthesized WS_2 nanostructures compared to a commercial bulk WS_2 powder exposed to the same intercalation and exfoliation conditions. (c) Nyquist plots show the corresponding trends in electrode kinetics. SEM images of the (d) as-received and (e) "exfoliated" bulk WS_2 powder show the much larger and irregular particles as compared to the CVD synthesized nanostructures. (f) Raman spectroscopy and (g) PXRD show that the "exfoliated" bulk powder remains mostly in its 2H phase.

To further understand the difference between different samples, we tried to drive the intercalation of bulk WS_2 powder more completely by going back to the more traditional oven-heating intercalation reactions, and further elevated the reaction temperature to 100 ^{o}C for 48 h in an autoclave (to mimize air leak and oxidation). This essentially follows the procedures recently reported by Voiry et al.[6c] This more stringest intercatlation reaction conidition clearly resulted in more complete intercalation and exfoliation as revealed by SEM (Figure S7c,d) and Raman (Figure S7e). Moreover, the electrochemical behaviors, the SEM, and the Raman spectra did not reveal much difference between the WS_2 nanosheets collected from the supernant or from the particles settled at the bottom after the exfoliation. This further suggests that these WS_2 samples were indeed thorougly exfoliated. Despite the more thorough exfoliation, there was still clear difference between the catalytic performance of the exfoliated 1T-WS_2 nanosheets originated from bulk power and CVD synthesized WS_2

nanostructures (Figure S7). The electrocatalytic current densities at the same overpotential is much lower than what was achieved by exfoliated 1T-WS_2 nanosheets made from CVD synthesized WS_2 nanostructures (Figure S7a), even though they are now similar to the values reported by Voiry et al.[6c] The EIS data (Figure S7b) reveal much higher charge transfer resistances (R_{ct}) of 51 Ω for the exfoliated 1T-WS_2 nanosheets made from the "everything" bulk WS_2 powder (the R_{ct} for the "supernanant" sample is 51 Ω) than that for exfoliated 1T-WS_2 nanosheets from the CVD synthesized (R_{ct} = 5 Ω). This comparison further underlines the benefits of using well controlled WS_2 nanostructures synthesized via CVD and suggests that the few-layer nanostructures with well defined crystalline edges enabled by our CVD synthesis promote better catalytical performance.

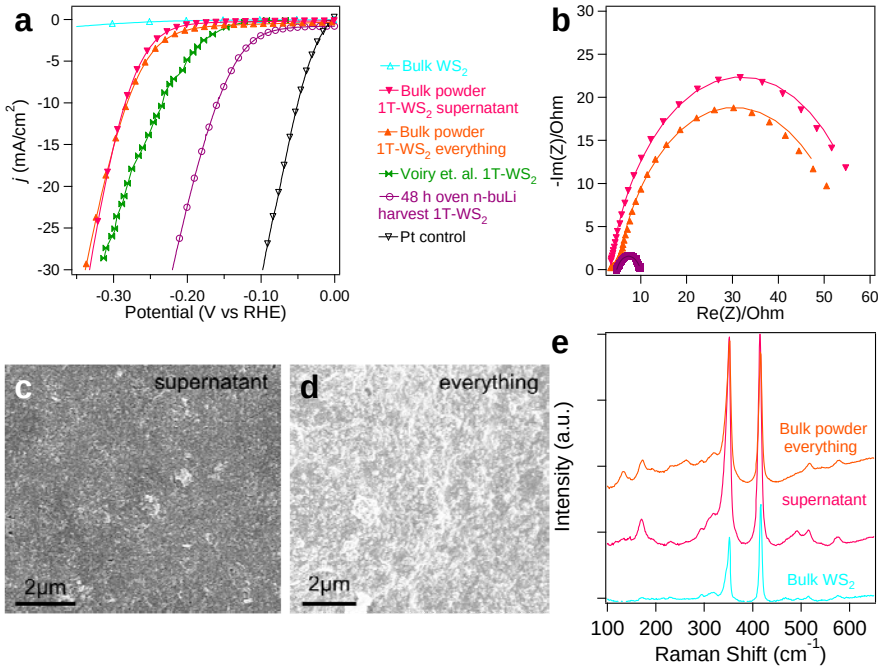

Figure S7. Comparison of the catalytic and electrochemical properties of exfoliated WS_2 nanosheets originated from the CVD synthesized WS_2 nanostructures and a commercial bulk WS_2 powder that have been exposed to intercalation at 100 °C for 48 h and identical exfoliation conditions. (a) Polarization curves showing the superior catalytic activity for chemically exfoliated nanosheets produced from CVD synthesized WS_2 nanostructures compared to the nanosheets from a commercial bulk WS_2 powder. (b) Nyquist plots show the corresponding trends in electrode kinetics for the WS_2 nanosheets exfoliated from the bulk WS_2 power and from CVD grown WS_2 nanostructures. SEM images of the (d) exfoliated WS_2 nanosheets taken from (c) the supernatant or (d) all of the materials at the bottom of the reaction vessel (called "everything") during the exfoliation process show both samples were

fully exfoliated without apparent large particles. (e) Raman spectroscopy confirms the emergence of Raman shifts associated with 1T-WS_2 phase after the exfoliation, similar to what was observed in Figure S1a.

VIII. Catalytic stability of exfoliated 1T-WS_2 nanosheets

We show the catalytic activity of 1T-WS_2 nanosheets is relatively stable although the 1T phase is metastable. We continously cycled the 1T-WS_2 nanosheets over 500 times under the normal operating conditions and monitored the catalytic performance (Figure S7a, b). In addition to monitoring the catalytic activity after continuous cycling, alternative stability test showed that the required potential to sustain a constant electrocatalytic current density of 10 mA/cm^2 increases by ~80 mV after 4 h of continuous catalytic hydrogen evolution reaction in 0.5 M H_2SO_4 (Figure S7c). The slight loss in catalytic activity is accompanied by an increase in charge transfer resistance, as revealed by EIS experiments (Figure S7d). This suggests a slow reconversion to the thermodynamically favored 2H polymorph and potential material loss from the surface of the graphite electrode could be responsible for the loss in catalytic activity.

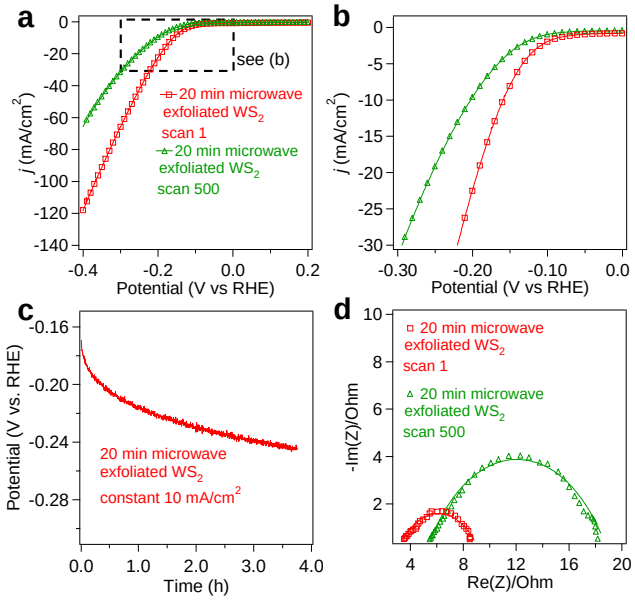

Figure S8. Polarization curves showing the catalytic stability of 1T-WS_2 nanosheets cycled continuously at (a) higher and (b) lower potentials. (c) The required potential to achieve a constant electrocatalytic current density of 10 mA/cm^2 is plotted against the time of continuous catalytic operation. (d) Nyquist plots show the slight increase in charge transfer resistance after continuous catalytic operation.